ARTICLE

Enhanced C-C coupling of Cu-based catalysts via zirconia-driven carbonate interaction for electrochemical CO_2 reduction reaction

Dayeon Kim [a], Hyewon Yun [a,b], Jiseon Kim [a,b], Chan Woo Lee [c], and Yun Jeong Hwang* [a,b]

Electrochemical CO_2 reduction (ECR) using Cu-based catalysts is a promising approach to producing C_{2+} chemicals such as C_2H_4 for sustainable carbon capture and utilization. Recent research has explored improving Cu catalyst performances through modifications, including integrating with other metal oxides. Here, we report that incorporating amorphous zirconia adjacent to copper oxide (CuO/ZrO_x) significantly improves its ECR performance in a membrane electrode assembly (MEA) electrolyzer. The CuO/ZrO_x catalyst exhibited a higher CO_2 adsorption capacity and increased current density for C_{2+} production compared to bare CuO. Specifically, the ethylene partial current density increased by 1.76 times. *Operando* X-ray absorption spectroscopy measurements reveal the evolution of the zirconia-carbonate interaction during ECR in the MEA, whereas the Cu state is reduced to the metallic state, irrespective of ZrO_2 presence. Post-reaction analysis shows that the modulation in the binding environment of Cu is associated with an increased oxidation state of Cu along with the enhanced interaction of CuO/ZrO_x with carbonate. These distinct properties support the role of zirconia in enhancing CO_2 affinity and mediating the reactant feed to the Cu-based catalyst surface.

Introduction

Electrochemical CO_2 conversion has been proposed as a sustainable carbon capture and utilization (CCU) method for carbon neutrality because of the advantage of using water as a proton supply.[1,2] The electrochemical CO_2 reduction reaction (ECR) enables the synthesis of various value-added chemicals at room temperature. C_{2+} chemicals including ethylene (C_2H_4) have been targeted, considering their large global market sizes and high prices.[1,2] Therefore, research has been extensively conducted to enhance C_{2+} production by investigating electrocatalysts, electrolytes, and electrolyzers.[3-5] Cu has been the most extensively studied element for C_2H_4 production due to its suitable intermediate binding energies for both *CO stabilization and C-C coupling reactions compared to other metal elements.[6,7] It has been demonstrated that oxide-derived Cu-based catalysts exhibit outstanding performance for C-C coupling compared to bare Cu catalysts.[8-10] More recent studies have reported that introducing add-layer components on the Cu-based catalyst surface can enhance C_{2+} production by adjusting the electronic state of the Cu or the local pH.[11] However, challenges such as suppressing the hydrogen evolution reaction (HER) or obtaining higher selectivity over C_1

chemicals such as CO or formate, still require improvement of the catalyst performance through the integration with other materials.[1,2]

The ECR occurs at the tri-phase interface, consisting of gaseous CO_2 reactants, liquid aqueous electrolytes, and solid catalyst surfaces. In a membrane electrode assembly (MEA) electrolyzer combined with a gas diffusion electrode (GDE), the catalyst on the cathode compartment can be directly supplied by gas-fed CO_2, resulting in ECR performance improvements due to the increased CO_2 availability to the catalyst surface.[12] However, in the anion exchange membrane (AEM) environment commonly used in MEA devices, an increase in local pH due to the formation of hydroxide ions (OH^-) during ECR leads to the conversion of CO_2 to (bi)carbonate, resulting in carbon loss and limiting CO_2 conversion efficiency.[13] This issue is exacerbated at higher current densities due to increased carbonate formation near the catalyst electrode, necessitating the development of suitable electrodes to work in these locally alkaline environments.[13] Strategies to develop suitable electrodes are done by introducing secondary components, such as organic moieties, polymers, and metal oxides, onto the catalyst surface which has been demonstrated to enhance the interaction with CO_2 molecules. The additional components can assist the catalytic active sites by multiple factors such as adjusting CO_2 adsorption, oxidation state of Cu, local pH, hydrophobicity, etc.

In particular, metal oxides have been widely utilized to modulate the electronic state and thus the catalytic activity for various reactions.[14-16] Metal oxides such as CeO_2, SiO_2, and Al_2O_3, which act as Lewis acids, can improve ECR selectivity by forming interfaces with the Cu-based catalyst.[11,14] The metal oxide is proposed to adjust the oxidation state of Cu or the

a. Department of Chemistry, Seoul National University, Seoul 08826, Republic of Korea
b. Center for Nanoparticle Research, Institute for Basic Science (IBS), Seoul 08826, Republic of Korea
c. Department of Chemistry, Kookmin University, Seoul 02707, Republic of Korea
* Correspondence: yjhwang1@snu.ac.kr

adsorption energy of CO_2 molecules or intermediates. Meanwhile, other contributions by metal oxide can be considered. Metal oxides such as MgO and ZrO_2 acting as Lewis bases have been developed as absorbents for CO_2, which directly facilitates the binding of CO_2 or carbonate.[16] To achieve conversion beyond capturing CO_2, reversible adsorption and desorption of CO_2 must occur. CO_2 binds to ZrO_2 with moderate strength compared to other metal oxides, allowing CO_2 desorption at room temperature.[17] Additionally, ZrO_2 exhibits high chemical stability, ensuring stability across a wide pH range and providing excellent cyclability.[18] ZrO_2, known to act as both Lewis acid and base, has been suggested to enhance CO_2 activation and thermochemical conversion performance when combined with copper catalysts.[19] Similarly, ZrO_2 may support the local supply of reactants to the active sites of Cu during the ECR. These research efforts highlight the interest in integrating metal oxides into ECR catalysts, and further studies are needed to understand their contribution to C-C coupling, especially when used with Cu catalysts.

Here, we demonstrate that introducing ZrO_2 into CuO can enhance the ECR performance of C_{2+} chemical production. Specifically, we observed a significant improvement in current density when amorphous ZrO_2 is present in a gas-fed GDE-based MEA environment compared to bare CuO. *In-situ/operando* X-ray absorption spectroscopy results pointed out that the electronic states of Zr interacted with carbonates, while Cu remained in a similar metallic state regardless of the presence of ZrO_2 during the ECR process at the MEA electrolyzer. This suggests that ZrO_2 aids in CO_2 activation and effectively has a carbonate form, which contributes to the supply of reactant to the catalyst surface. Post-reaction analysis of the CuO/ZrO_x indicates an increased carbonate signal, a noticeable increase in the distribution of Cu^{2+} species, and changes in the bonding environment of Cu compared to the CuO, supporting the carbonate-mediated chemical interaction at the interface. Our study demonstrates that incorporating metal oxides can increase the ECR performance mediated by carbonate interaction, which can be utilized to design efficient catalysts for electrochemical CO_2 conversion.

Experimental

Materials

Copper(II) nitrate trihydrate ($Cu(NO_3)_2 \cdot 3H_2O$, puriss. p.a., 99–104%), sodium hydroxide (NaOH, ACS reagent, ≥97.0%, pellets), sodium carbonate (Na_2CO_3, powder, ≥99.5%, ACS reagent), zirconium(IV) carbonate hydroxide oxide (≥40% ZrO_2 basis), copper(II) oxide (CuO, nanopowder), copper(I) oxide (Cu_2O, nanopowder), potassium bicarbonate ($KHCO_3$, ≥99.95%), isopropanol (IPA, ACS reagent ≥99.5%), Nafion™ ionomer (~5% in a mixture of lower aliphatic alcohols and water) were purchased from Sigma Aldrich. Zirconium dinitrate oxide hydrate ($ZrO(NO_3)_2 \cdot xH_2O$, 99.9%, metals basis), iridium(IV) oxide (IrO_2, Premion®, 99.99%) were purchased from Alfa Aesar. Ethanol (99.9%) was purchased from Samchun Chemicals (Korea). Platinized titanium screen mesh and gas diffusion layers (GDL, Sigracet 39 BB, SGL Carbon) were purchased from the Fuel Cell Store. The spray gun (Gunpiece GP-2) was purchased from Fuso Seiki. MEA-type CO_2 electrolyzer (5 cm^2 scale) and Sustainion® X37-50 Grade RT membrane were purchased from Dioxide Materials.

Catalyst synthesis

For the synthesis of CuO/ZrO_x, 0.4832 g of $Cu(NO_3)_2 \cdot 3H_2O$ was dissolved into 10 mL of water, and 10 mL of 0.5 M NaOH solution was added dropwise under vigorous stirring. After stirring for 30 min, 2 mL of 0.2 M $ZrO(NO_3)$ solution was injected into the solution. After stirring for 10 min, 20 mL of 0.1 M Na_2CO_3 was injected into the solution for the precipitation. After stirring for 20 min, the product was washed three times with IPA (centrifuge, 8000 rpm, 10 min, 15 ℃). The product was dried under vacuum at room temperature overnight. The blue powder after drying was calcinated at 200 ℃ with a ramping rate of 10 ℃/min and maintained for 1 hr under the Ar atmosphere. CuO, CuZrO-0.5, and CuZrO-2 catalysts were synthesized by following a similar procedure described above, except the amounts of zirconium precursor and Na_2CO_3. 0 mL, 1 mL, and 4 mL of 0.2 M $ZrO(NO_3)_2$ solution were added to form CuO, CuZrO-0.5, and CuZrO-2, respectively. Also, 20 mL, 10 mL, and 40 mL of 0.1 M Na_2CO_3 solution were added to form CuO, CuZrO-0.5, and CuZrO-2, respectively.
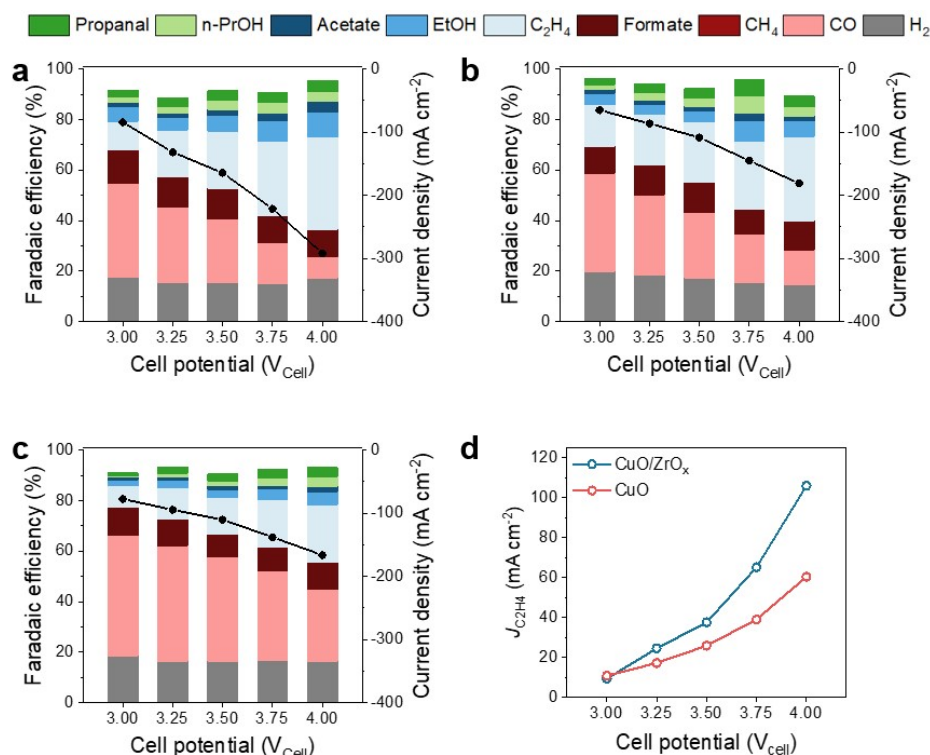
Material Characterization

Fig. 1 ECR performance of CuO/ZrO$_x$ and CuO catalysts in MEA electrolyzer with 0.1 M KHCO$_3$ electrolyte. (a) The FEs for products and total current densities on CuO/ZrO$_x$, (b) CuO, and (c) physically mixed CuO+ZrO$_x$ catalysts at different cathodic potentials. (d) Comparison of the partial current densities for C$_2$H$_4$ on CuO/ZrO$_x$, and CuO catalysts.

To take the morphological and elemental analysis over the synthesized particles, a transmission electron microscope (TEM; JEM-F200(TFEG)) operating at 200 kV and a Cs-scanning transmission electron microscope (STEM; JEM-ARM200F) operating at 200 kV were employed. High-resolution transmission electron microscopy (HRTEM) images, selected area electron diffraction patterns, high-angle annular dark-field (HAADF) images, and energy dispersive spectroscopy (EDS) mapping images were also obtained. To identify the crystal structure of each catalyst, X-ray diffraction (XRD) analysis was performed using Bruker D8-Advance with Cu target (λ = 1.54056 Å) at room temperature. The inductively coupled plasma optical emission spectroscopy (ICP-OES; Agilent ICP5800) system was employed to analyze the elemental contents of the catalysts. To confirm the surface oxidation state of components, X-ray photoelectron spectroscopy (XPS) analysis was conducted by Thermo Electron Corporation K-ALPHA +, using Al Kα X-ray radiation (1486.6 eV) for excitation. Fourier transform infrared (FT-IR) spectra were obtained with Bruker TENSOR27 equipped with a high sensitivity of deuterated L-alanine-doped triglycine sulfate (DLATGS) detector and using a high energy air-cooled mid-infrared glower source as the IR source. X-ray absorption spectroscopy (XAS) measurements at Cu K-edge and Zr K-edge were performed for *ex-situ* and *in-situ/operando* analysis at the 10C beamline of Pohang Acceleration Laboratory (PAL) in South Korea. To analyze the obtained data from XAS, the Athena software was used. The extended X-ray absorption fine structure (EXAFS) spectrum was transformed using the Kasier-Bessel function. Morlet wavelet transform EXAFS data were analyzed using MATLAB software.

Electrochemical CO$_2$ reduction reaction performance

To measure the electrochemical CO$_2$ reduction performance of the catalysts, a zero-gap MEA-type CO$_2$ electrolyzer was used. The cathode was fabricated by spraying 0.5 mg cm^{-2} of ink onto the GDE carbon paper (Sigracet 39BB). The cathode ink was prepared by mixing 6.0 mg of catalyst with 1 mL of IPA and 60 μL of Nafion ionomer, followed by sonication for 30 min. The anode was fabricated by spraying IrO$_2$ ink onto platinized Ti mesh. The IrO$_2$ ink was prepared by mixing 30 mg of IrO$_2$ with 1 mL of IPA and 300 μL of Nafion ionomer, followed by sonication for 30 min. The prepared cathode was used as the working electrode and the anode was used as the counter electrode separated by an AEM (Sustaintion membrane). This experiment utilized a 2-electrode system, and the cell potential was applied using a potentiostat (Ivium potentiostat). During the ECR measurement, high-purity CO$_2$ gas (99.999%) continuously passed through a humidifier to attain 100 % relative humidity and flowed over the cathode electrode at a flow rate of 100 sccm. Meanwhile, 0.1 M KHCO$_3$ electrolyte was circulated over the anode electrode at 17 rpm using a peristaltic pump.

The gas products were analyzed using gas chromatography (GC, Agilent), and the liquid products were quantified using ^{1}H-nuclear magnetic resonance spectroscopy (NMR, 500MHz Bruker). The GC was equipped with a Carboxen 1000 column (Supelco), and high-purity Ar gas was used as the carrier gas. The gas product was injected into the GC every 15 min, where H$_2$ and CO were detected using a thermal conductivity detector (TCD), and CH$_4$ and C$_2$H$_4$ were detected using a flame ionization detector (FID). For liquid products, 1 mL of anolyte was sampled every 15 min. From each sample, 450 μL was taken and mixed

with 50 µL of an internal standard solution. The standard solution consisted of dimethyl sulfoxide (DMSO) and phenol in D_2O. Ethanol, acetate, n-propanol, and propanal were quantified based on their intensity relative to the DMSO peak, while formate was quantified based on its intensity relative to the phenol peak. The Faradaic efficiency (FE) of each gas product was calculated using the equation.

$$FE_{product\ i} = x_i \times v \times \frac{z_i F P_0}{RT} \times \frac{1}{I_{total}} \times 100\%$$

where x_i represents the volume fraction of product i, v represents the flow rate of CO_2 gas, and z_i is the number of electrons consumed when CO_2 is reduced to product i. F is the Faradaic constant, P_0 is the pressure, 101325 Pa. R is the ideal gas constant, T is the temperature, and I_{total} is the measured total current. The FE of each liquid product was calculated using the equation below, where n_i is the produced amount (mole) of the liquid product i that is quantified by NMR analysis, and Q is the total passed charged during the ECR.

$$FE_{product\ i} = \times \frac{z_i F}{Q} \times 100\%$$

Openrando X-ray absorption Spectroscopy in MEA

For *in-situ/operando* XAS analysis in MEA, a custom-made MEA electrolyzer was utilized. To obtain the signal at the fluorescence mode during ECR, the *operando* MEA cell had a window on the cathode side sealed with Kapton tape to allow the X-ray incident beam to pass through. The electrode preparation conditions, electrolyte, gas flow rate, and liquid flow rate were the same as for the ECR performance measurements. XAS analysis was performed under open circuit potential (OCP), 3 V of the cell voltage (3 V_{cell}), and post-ECR conditions for Cu K-edge and Zr K-edge, respectively. Commercial CuO, Cu_2O, Cu foil, and synthesized $Cu(OH)_2$ were used as Cu references, and commercial $Zr(OH)_2CO_3 \cdot ZrO_2$, ZrO_2, and Zr foil were used as Zr references.

Results and discussion

ECR measurement in MEA

To determine whether introducing zirconia (ZrO_x) contributes to ECR using Cu-based catalysts, we prepared CuO/ZrO_x catalysts and compared their performance through product analysis at various operating potentials (Figure 1). To investigate whether ZrO_x modulates the C-C coupling activity, oxide-derived Cu catalysts were incorporated with ZrO_x, and ECR performances were measured in the MEA electrolyzer. CuO, CuO/ZrO_x, and ZrO_x were synthesized following the procedure in Scheme S1, with catalyst characterization discussed later. For performance comparison, a carbon-based GDE was used to load synthesized CuO/ZrO_x and CuO catalysts at the same loading amount (0.5 mg cm^{-2}), so that a smaller amount of Cu was loaded into the CuO/ZrO_x compared to the bare CuO catalyst electrode. ICP OES analysis showed that the atomic ratio of Cu: Zr in CuO/ZrO_x was approximately 5:1 (Table S1). The total current density (j_{total}) increased with the ZrO_x introduction, especially improving the

partial current density for C_2H_4 production (j_{C2H4}) by 1.76 times at an operating voltage of 4.0 V. The ethylene selectivities of CuO/ZrO_x and CuO at 4.0 V were 36.4% and 33.3%, respectively. The introduction of ZrO_x did not significantly affect product selectivity but showed a substantial improvement in total current density. To investigate the improvement in current density, EIS experiments were conducted (Figure S1). R_{CT} values of the CuO/ZrO_x and the CuO catalyst exhibited 49.34 Ω and 58.66 Ω, respectively. This indicates that the presence of ZrO_x lowers the charge transfer resistance, potentially accelerating the reaction rate.

Both catalysts showed similar FEs for hydrogen production over the various applied potentials. At the same time, mainly CO was produced at lower cell voltages (< 3.5 V), while higher cell voltage increased C-C coupling, enhancing FE for C_{2+} products. Although the FEs of ECR reaction products were similar for both catalysts, ZrO_x presence resulted in slight improvements in the FEs for C_2H_4 and C_2H_5OH (Figures 1a and 1b). For comparison, ZrO_x was synthesized following the same method (Figure S2) and physically mixed with CuO, whose ECR of the simple mixture catalyst exhibited rather increased CO production and decreased C-C coupling both in FE and current density compared to CuO alone (Figure 1c). This suggests that the
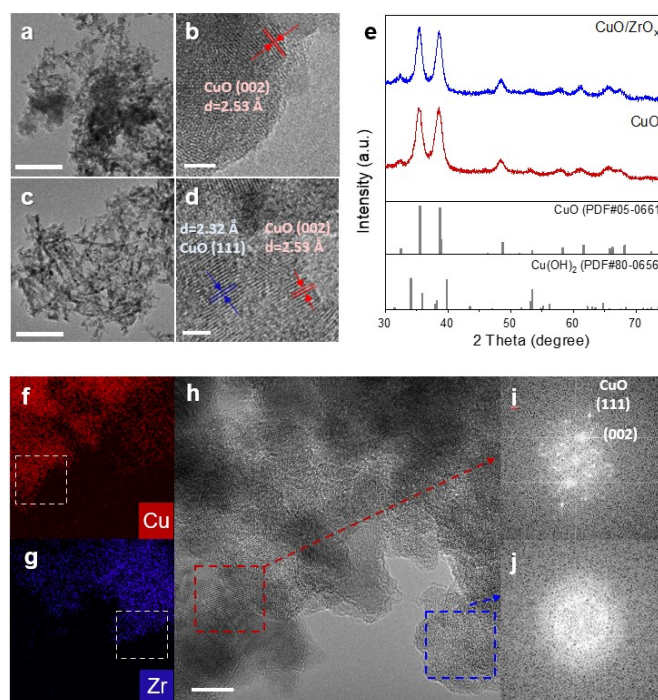

interface formation in CuO/ZrO_x during catalyst preparation enhances C-C coupling. In contrast, physical mixing results in decreased performance towards C_2H_4 production. This result is due to the difficulty in achieving an ensemble effect with Cu catalysts, where the proximity of active Cu sites is effective for

Fig. 2 Characterizations of as-prepared CuO/ZrO_x and CuO catalysts. **a-b** (a) TEM, (b) HR-TEM image of CuO/ZrO_x. **c-d** (c) TEM, (d) HR-TEM image of CuO. (e) XRD patterns of CuO/ZrO_x and CuO. **f-j** (f), (g) TEM-EDS, (h) HR-TEM, (i), (j) FFT images of CuO/ZrO_x. Scale bars correspond to 200 nm in (a), (c), 2 nm in (b), (d), and 5 nm in (h).

C-C bonding. If ZrO_x is mixed and does not interact with Cu catalyst, it could increase the distance between Cu sites,

lowering C_{2+} formation efficiency and rather increasing CO selectivity. A significant performance improvement with Cu/ZrO_x was obtained in total current density, enhancing partial current densities of C_2H_4 and C_{2+} products compared to bare CuO (Figures 1d and S3).

To further investigate the effect of ZrO_x, we adjusted the amount of Zr introduced into the catalyst to 0.5 and 2 times (denoted as CuZrO-0.5 and CuZrO-2, respectively) and compared their ECR performances (Figure S4). The Cu: Zr ratio in CuO/ZrO_x is controlled by the amount of added Zr precursor, and ICP analysis shows similar ratios in synthesized catalysts (Table S1). All Zr-incorporated catalysts showed a noticeable increase in current density compared to CuO. A cell voltage of 4.0 V achieved a total current density near 300 mA/cm². The product distribution was influenced by Zr amounts, with CuO/ZrO_x showing the highest $j_{C_2H_4}$. Although CuZrO-0.5 also increased $j_{C_2H_4}$ compared to CuO, CuZrO-2 samples showed decreased C_2H_4 selectivity and increased HER. This indicates that high ZrO_x amounts lower ECR selectivity. The comparative experiments confirmed that when a suitable amount of ZrO_x was introduced, the partial current density for C-C coupling was enhanced compared to the bare CuO.

Characterization of CuO/ZrO_x

Next, to understand the improved activity, we performed the material analysis of the catalysts before, during, and after the reaction. Material characterizations of as-prepared catalysts were conducted using TEM and XRD analyses, which exhibited that crystalline CuO and amorphous ZrO_x nanostructures were well-dispersed, and ZrO_x was adjacent to CuO (Figure 2). As mentioned earlier, we incorporated ZrO_x into copper oxides to verify ZrO_x effects since various copper oxides such as $Cu(OH)_2$, Cu_2O, and CuO are known to induce active morphologies (e.g., grain boundaries) for C-C coupling when reduced to Cu during ECR.[9-10] Therefore, the CuO/ZrO_x interface was introduced by sequential precipitation of Cu and Zr precursors and subsequent heat treatment. The CuO catalyst was prepared under the same synthesis and heat treatment conditions without Zr precursors. TEM images of CuO/ZrO_x and CuO show the morphologies in Figures 2a-b, and 2c-d, respectively. The overall morphology of the two catalysts is similar (Figures 2a and 2c), with domains of small particles around 10 nm overlapping each other. The HRTEM images of both catalysts show the lattice fringes of 2.53 and 2.32 Å, corresponding to monoclinic CuO (002) and CuO (111), respectively. The selected area electron diffraction (SAED) patterns correspond to the ring pattern of the CuO crystal structure, but no significant features associated with the crystalline structure of ZrO_2 are observed (Figure S5).

Fig. 3 Electronic structure characterization studies of CuO/ZrO_x and CuO. (a) Cu 2p, (b) O 1s XPS spectra of CuO/ZrO_x and CuO catalysts. (c) Zr 3d XPS spectrum of CuO/ZrO_x catalyst. **d-e** *ex-situ* (d) Cu K-edge XANES and (e) EXAFS of CuO/ZrO_x and CuO catalysts. **f-g.** *ex-situ* (f) Zr K-edge XANES and (g) EXAFS of CuO/ZrO_x catalyst.
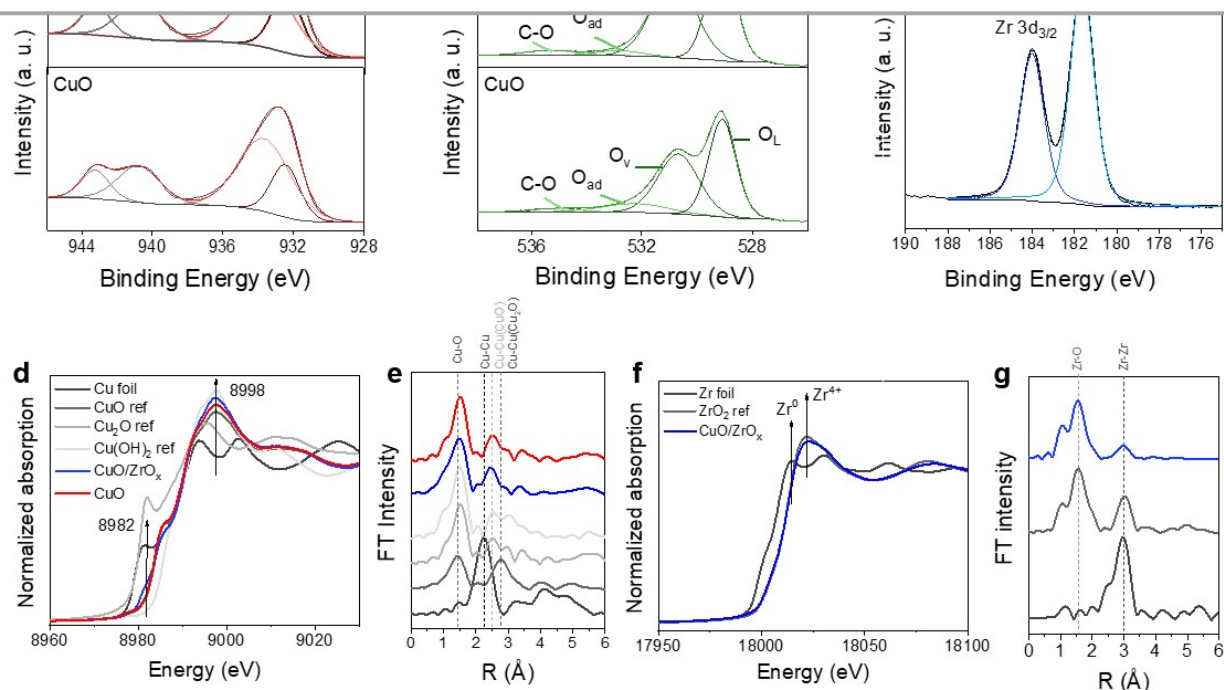
The XRD patterns are consistent with the TEM crystal analysis, having peaks associated with the monoclinic CuO (JCPDS card no. (05-0661)) structure (Figure 2e). Additionally, the broad XRD patterns indicate small crystalline domains of CuO, consistent with the HRTEM image results. The same full width at half maximum (FWHM) in both catalysts indicates that the average size of the CuO domain is similar. Patterns corresponding to

Cu(OH)$_2$ are not observed, indicating that the catalyst obtained after the calcination at 200°C has a CuO structure. The absence of additional peaks in CuO/ZrO$_x$ compared to CuO points out the amorphous ZrO$_x$ characteristics. This aligns with previous reports, which state that after Zr precipitation, annealing at high temperatures (> 300°C) yields tetragonal or monoclinic ZrO$_2$ crystalline structures, while lower temperature tends to produce an amorphous structure.[19] Previous research reported that CO$_2$ binds weaker to amorphous zirconia compared to crystalline zirconia.[18] This weaker binding might be favourable for our catalyst, as reversible adsorption and desorption of CO$_2$ are desirable for conversion.

To further observe the distribution of elements within the particles, STEM EDS mapping images were obtained, revealing that Cu and Zr were well-dispersed (Figures 2f-h and S5). However, there are regions enriched in Cu (Figure 2f) and regions enriched in Zr (Figure 2g). The FFT images of the Cu-rich region display CuO patterns (Figure 2i), while the lack of characteristic patterns in the Zr-rich region supports the amorphous nature of ZrO$_x$ (Figure 2j), consistent with the XRD results.

Fig. 4 Evolution of the XAS under ECR in the MEA cell. *In-situ* (a) Cu K-edge XANES, (b) EXAFS of CuO/ZrO$_x$ and CuO catalysts in the MEA cell. *In-situ* (c) Zr K-edge XANES spectra and (d) Zr K-edge *in-situ* EXAFS spectra of CuO/ZrO$_x$ in the MEA cell.

Next, the electronic states of CuO/ZrO$_x$ and CuO were investigated using XPS and *ex-situ* XAS (Figure 3 and Figure S6). The high-resolution Cu 2p XPS spectra reveal that both as-prepared CuO/ZrO$_x$ and CuO catalyst surfaces have similar oxidation states with a broad Cu 2p$_{3/2}$ signal. The deconvoluted features have characteristic binding energies at 932.3 eV and 933.6 eV, corresponding to Cu$^{+/0}$ and Cu^{2+}, respectively[20], and their ratio is nearly identical in both catalysts. The Cu Auger spectra did not show distinct features corresponding to Cu^0, indicating that Cu 2p mainly comprises oxidized Cu$^+$ or Cu^{2+} states (Figure S8).[21] The Cu$^+$ species can be observable when the CuO surfaces have oxygen vacancies.[22] These Cu 2p XPS results showing the coexistence of Cu$^+$ and Cu^{2+} indicate that our synthesized catalysts have defective surfaces. The O 1s XPS spectra exhibit a high proportion of oxygen vacancy (O$_v$) features, and these vacancies are also obtained when ZrO$_x$ is introduced in CuO (Figure 3b). Furthermore, the Zr 3d XPS spectrum of Cu/ZrO$_x$ catalyst reveals the oxidation state of Zr^{4+} with the peaks at 184.0 eV and 181.4 eV, corresponding to the 3d$_{5/2}$ and 3d$_{3/2}$, respectively (Figure 3c).[23] The XPS spectra also identify that the atomic ratio of Cu: Zr on the catalyst surface is 0.85:0.15, consistent with the ICP analysis result.

Ex-situ Cu K-edge XANES confirms that both catalysts predominantly exhibit the character of CuO, and the Zr introduction shows a minor spectral distortion (Figure 3d). The synthesized CuO catalyst features characteristic absorption signals at 8986 eV and 8998 eV, closely resembling the XANES of the CuO reference. These correspond to electron transfers from Cu^{2+} 1s $\rightarrow$ 4p$_{xy}$ and 1s $\rightarrow$ 4p$_z$, respectively, matching well with the monoclinic CuO which has a square planar structure with four oxygen coordination.[24] The edge-peak of Cu$_2$O at 8982 eV, indicative of Cu$^+$ 1s $\rightarrow$ 4p$_{xy}$ electron transfer,[24] was not observed in our synthesized CuO catalyst. This absence indicates CuO as the dominant structure in our synthesized catalyst. Interestingly, the Cu K-edge XANES spectrum of the CuO/ZrO$_x$ catalyst shows a slight increase in the edge-peak at 8982 eV, while the edge-peak intensity at 8986 eV for Cu^{2+} decreases and the white-line peak intensity at 8998 eV for Cu^{2+} increases, compared to the CuO catalyst. This indicates that Zr introduction causes orbital distortion of Cu,[25] suggesting electronic interaction between adjacent Cu and Zr. The Cu K-edge EXAFS spectra show that the characteristic features of Cu-O and Cu-Cu in the synthesized catalyst are consistent with the CuO reference (Figure 3e). Meanwhile, the wavelet transform (WT) of the *k^2*-weighted Cu EXAFS spectra described in Figure S9, can provide radial distance and *k*-space resolution, clearly reflecting structural information. This enables precise identification of structural details around different atoms in complex mixed structures.[26,27] The WT intensity peaks at the expected positions for heavy atoms such as Zr and Cu (6-8 (Å^{-1})) are absent, indicating that Cu-related bonds in the CuO/ZrO$_x$ catalyst are Cu-O and Cu-Cu, with no evidence of Cu-Zr bonds.[28] Additionally, the Zr K-edge XANES and EXAFS spectra show that the Zr species in the as-prepared CuO/ZrO$_x$ catalyst exhibit characteristic signals closely matching those of ZrO$_2$ (Figure 3f-g). These various material characterization results show that the synthesized CuO/ZrO$_x$ catalyst consists of a mixture of CuO
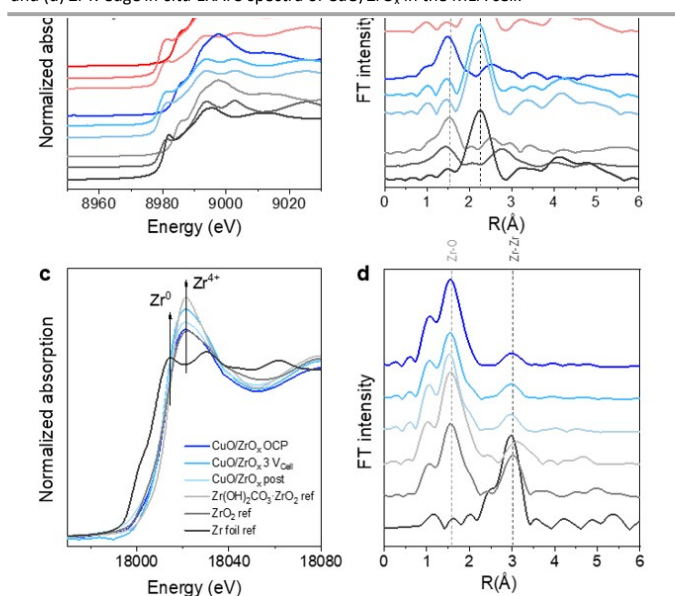
nanocrystals and amorphous ZrO_2, well-dispersed and adjacent to each other.

In-situ/operando studies of CuO/ZrOₓ in MEA

It is well known that the state of the active Cu site during the ECR has a significant effect on determining C-C coupling activity.[9] To investigate the correlation between the electronic state of Cu-based catalysts and their ECR activity, in-situ/operando XAS experiments were performed with the MEA electrolyzer. The Cu K-edge XANES spectra show that the CuO state is maintained in both CuO/ZrOₓ and CuO under open circuit potential (OCP) conditions in the MEA. However, when a negative potential is applied, the Cu K-edge XANES of both catalysts transforms to the Cu^0 state (Figure 4a). Consistently, the characteristic peaks of the Cu K-edge EXAFS spectra of CuO/ZrOₓ and CuO exhibit a feature corresponding to the Cu-O bond under OCP, which shifts to Cu-Cu bonds upon operando ECR condition (Figure 4b). The identical Cu states for both catalysts under operando conditions show that Cu is sufficiently reduced, and Zr does not significantly influence the electronic states of Cu during the ECR. The reduction of copper oxide to Cu^0 during the ECR is well-studied.[9,10] In addition, the catalyst maintains the Cu^0 state right after the ECR in the MEA, while the ex-situ samples show partial oxidation to Cu_2O according to Cu K-edge XANES due to air exposure (Figure S10). The evolution of Cu_2O after the ECR has been reported in copper oxide catalysts.[10] Consistently, XRD patterns of our catalysts show the disappearance of CuO peaks and the appearance of Cu_2O peaks (Figure S11), and HR-TEM images display lattice fringes corresponding to Cu_2O (Figure S12). Previous studies of Cu catalysts modified with metal oxide have reported that the metal oxide contributes to C_{2+} production by inducing a partial oxidation of Cu during ECR.[29] However, in our catalyst, we speculated that ZrOₓ might have another role because the introduction of ZrOₓ improves the current density without affecting Cu species during the reaction.

Although the introduction of Zr does not modulate the electronic state of Cu, in-situ/operando XAS of the Zr K-edge on CuO/ZrOₓ are analyzed to investigate whether any chemical changes in Zr are involved during the ECR. At OCP, the catalysts maintained the ZrO_2 state, consistent with ex-situ analysis. Notably, upon applying the cathodic potential, the white-line peak intensity of Zr^{4+} increases toward the XANES features of the $Zr(OH)_2CO_3 \cdot ZrO_2$ reference (Figure 4c). When CO_2 binds to the oxygen sites of zirconia, it can be adsorbed in the form of carbonate.[17] This suggests that ZrOₓ can interact with CO_3^{2-}/CO_2, forming $Zr(OH)_2CO_3$ during the reaction. Zr EXAFS confirms that Zr species do not transform into metallic Zr under reduction potential, as the intensity of Zr-Zr bonds does not increase and the intensity of Zr-O bonds is preserved. The EXAFS spectra for the $Zr(OH)_2CO_3$ and ZrO_2 references are nearly identical because carbon forms a bond through the oxygen of zirconia (Figure 4d). To investigate how the formation of zirconium carbonate can mediate the ECR activity enhancement, we additionally performed surface analysis of the post-ECR catalysts.

Improved carbonate/CO₂ affinity

The FT-IR spectra support that CuO/ZrOₓ is notably carbonate-rich compared to CuO in the post-ECR samples (Figure 5a). As previously discussed (Figure S10-12), Cu_2O is formed when the two catalysts are exposed to air after ECR. The FT-IR spectra also show a peak at 619 cm^{-1} corresponding to Cu_2O.[30] Both catalysts exhibit peaks at 1395 cm^{-1}, 830 cm^{-1}, and 702 cm^{-1}, representing the v_3 asymmetric vibration mode, v_2 asymmetric vibration mode, and v_4 symmetric vibration mode of carbonate, respectively.[31] Relative to the Cu_2O peak intensity, the intensity of carbonate peaks is higher in the post-ECR CuO/ZrOₓ catalyst than the post-ECR CuO, indicating that the Zr introduction enriches the catalyst surface with carbonate.

Meanwhile, TEM-EDS analysis on the post-ECR catalyst shows that Cu and Zr remain well interfaced after the reaction. In the post-ECR TEM-EDS images of CuO/ZrOₓ, the purple region
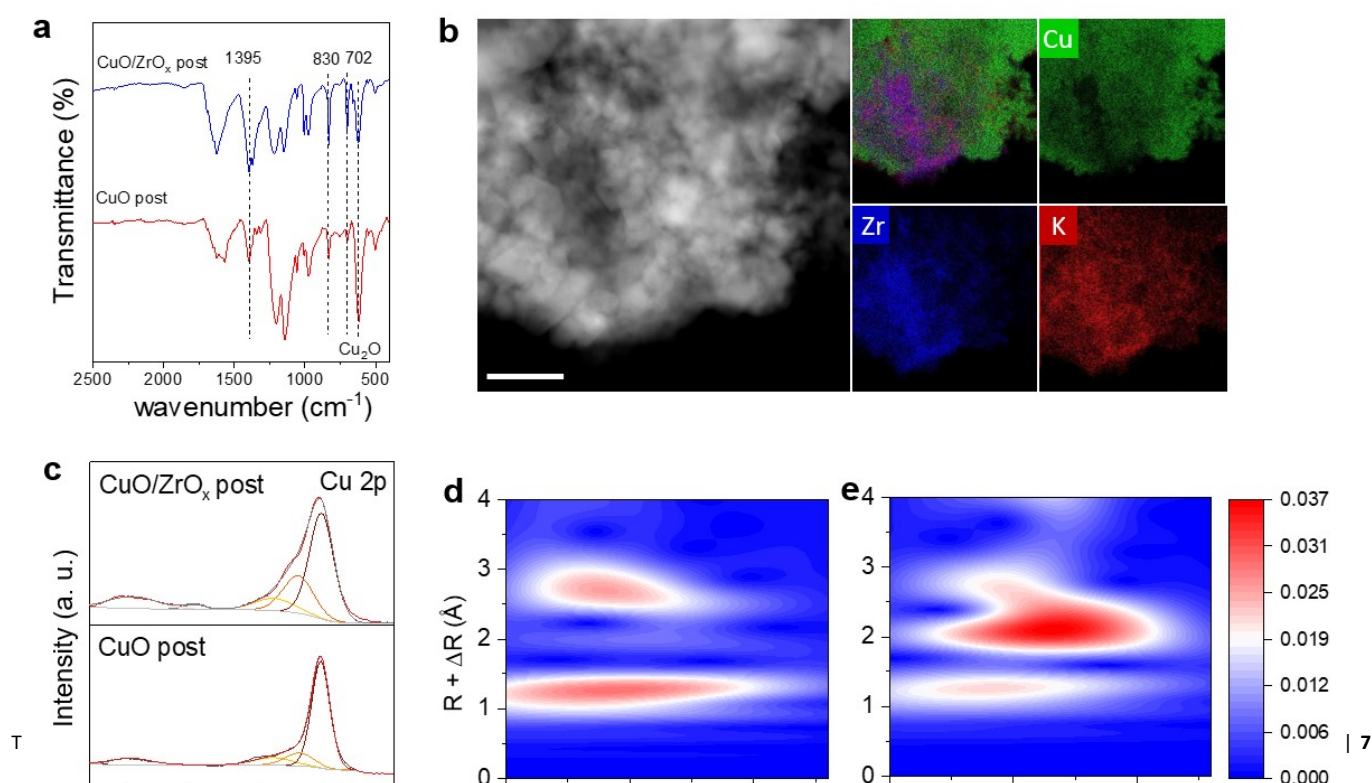

Fig 5. (a) FT-IR spectra of CuO/ZrOₓ and CuO catalysts post ECR. (b) STEM-EDS images of the CuO/ZrOₓ catalyst post-ECR. The image where green, blue, and red all appear is an overlay of the distributions of Cu, Zr, and K. (c) Cu 2p XPS spectra of CuO/ZrOₓ and CuO catalysts post ECR. **d-e** Wavelet transform spectra of (d) CuO/ZrOₓ and (e) CuO post ECR. Scale bars correspond to 100 nm in (b).

indicates the overlap of the blue (Zr) and red (K) distributions. There is a notable overlap between K and Zr distributions, while Cu shows an independent distribution from K, indicating a possible carbonate enrichment in the Zr-rich region (Figure 5b). In contrast, the post-ECR TEM-EDS image of CuO shows a uniform distribution of Cu and K (Figure S13). The characteristic distribution of K can be attributed to the Lewis acid sites on Zr, which can draw carbonate and attract K^+ from the electrolyte. These FT-IR and TEM analyses support that the introduction of Zr can enhance the carbonate affinity of the catalyst. Furthermore, CO_2 Brunauer–Emmett–Teller (BET) measurements revealed that CuO/ZrO_x has a 1.25 times higher CO_2 adsorption capacity than CuO (Figure S14). CuO/ZrO_x enhances the affinity not only for carbonate but also for CO_2.

Then, Cu 2p XPS analysis was performed on the post-ECR catalysts to investigate whether the abundant carbonate on the catalyst surface can also interact with Cu (Figure 5c and Figure S6c-d). Herein, both post-ECR CuO/ZrO_x and CuO catalysts show significantly different Cu 2p XPS features than before the reaction (Figure 3a). Also, the peak intensity corresponding to the high binding energy is notably increased on the Zr-introduced catalyst. Both catalysts commonly exhibit a strong $Cu^{+/0}$ feature at 932.3 eV, indicating the formation of a Cu/Cu_2O mixture after ECR. In addition, Cu^{2+} features are identified at 933.6 eV and 935.1 eV, corresponding to CuO and $Cu(OH)_2/CO_3$, respectively.[20,32] Although the 932.3 eV peak is the major feature for both catalysts, the relative peak intensity of the Cu^{2+} species is higher on the CuO/ZrO_x surface, suggesting that the carbonate-abundant surface promotes Cu^{2+} species formation after ECR. Scheme S2 suggests that Cu sites interacting with carbonate form Cu^{2+} species that can reversibly convert between $CuCO_3$ and CuO upon air exposure.[33] In contrast, in the absence of carbonate, it has been reported that metallic Cu sites transform into a Cu_2O layer when exposed to air. Thus, the CuO/ZrO_x catalyst with a carbonate-rich surface exhibits relatively large Cu^{2+} peaks compared to the $Cu^{+/0}$ peak. Meanwhile, the CuO catalyst with a carbonate-poor surface appears to have metallic Cu and Cu_2O as the major species after the reaction. *Ex-situ* Cu K-edge EXAFS analysis reinforces them, showing major Cu-Cu bonds in post-ECR CuO catalyst and predominant Cu-O bonds in post-CuO/ZrO_x catalyst (Figure S10). XRD also shows a minor metallic Cu (200) peak at 50.4 degrees in the post-ECR CuO catalyst (Figure S11). The first-derivative maximum peaks of CuO post-ECR were slightly shifted compared to CuO/ZrO_x post-ECR to lower energies, indicating a larger ratio of metallic Cu (Figure S15). This is also confirmed by the wavelet transformation of *ex-situ* Cu K-edge EXAFS (Figure 5d-e). The contour of CuO/ZrO_x occupies one k-space at ~ 4 $Å^{-1}$, which is in good agreement with the Cu-Cu contour of copper oxides.[34] Meanwhile, the contour of the CuO catalyst occupies one k-space at ~ 7.0 $Å^{-1}$, which is well aligned with the Cu-Cu contour of Cu foil.[34] For both catalysts, a contour corresponding to Cu-O appears at ~4 $Å^{-1}$, and it is noteworthy that the contour of CuO/ZrO_x is more skewed downward and occupies a larger area. Based on a previous report that $CuCO_3$ has a shorter first shell radius compared to Cu_2O and CuO,[35] the downward expansion of the contour in the wavelet

transformation image suggests that Cu surface is interacting with carbonate. Taken together, this suggests that the interaction of zirconium carbonate affects the adjacent Cu surface, resulting in a carbonate-rich environment after ECR.

We propose the following mechanism for the chemical transfer from ZrO_x to Cu (Scheme 3). It has been reported that ZrO_x can undergo the adsorption/desorption of CO_2 by pressure swing at room temperature.[17] The carbonate formed on the zirconia surface can be reversibly desorbed into CO_2 when the surrounding CO_2 concentration decreases. Thus, ZrO_x acts as a reservoir, adsorbing CO_2 as carbonate and releasing it when the CO_2 level on the neighbouring Cu surface drops due to CO_2 consumption as a reactant during the ECR. The high carbonate/CO_2 affinity of ZrO_x can assist in supplying CO_2 to the active sites during the reaction, contributing to an increase in ECR current density in our CuO/ZrO_x. This characteristic is expected to be utilized in the design of high-performance ECR catalysts.

Conclusions

In this study, we demonstrated the significant enhancement of ECR performance by incorporating amorphous zirconia into the CuO catalyst. CuO/ZrO_x had a 1.76-fold increase in ethylene partial current density. Our findings from *in-situ/operando* XAS revealed that ZrO_x interacts with carbonates during the ECR process. The ability of ZrO_x to interact with carbonate is proposed to act as a reservoir that enhances C-C coupling activity by supplying CO_2 reactant to the Cu surface. Post-reaction analysis confirmed that the presence of ZrO_x leads to an enriched carbonate surface, promoting Cu^{2+} species formation and enhancing the overall carbonate-mediated chemical interaction at the catalyst surface. The improved CO_2 adsorption capacity of the CuO/ZrO_x catalyst compared to bare CuO further supports the role of ZrO_x in enhancing CO_2 affinity and ECR performance. The integration of zirconia into Cu-based catalysts provides a promising strategy for enhancing the efficiency of electrochemical CO_2 conversion. Beyond adjusting the oxidation state or forming grain boundaries, we suggest that combining foreign metal oxides can affect the catalyst interaction with carbonate/CO_2 species and therefore propose a new route to improve ECR catalytic activity.

Author contributions

D. K. designed and performed all experiments and write the manuscript. H. Y. conducted XAFS data fitting and WT data analysis. H. Y. and J. K. supported *in-situ/operando* XAS experiments. C. W. L. assisted in the synthetic approach and catalyst characterization. Y. J. H. supervised the project and write the manuscript. All authors contributed to the discussion of data and the edition of the manuscript.

Conflicts of interest

The authors declare no competing financial interest.

Data availability

The data supporting this article have been included as part of the Supplementary Information.

References

1. S. Nitopi, E. Bertheussen, S. B. Scott, Xi. Liu, A. K. Engstfeld, S. Horch, B. Seger, I. E. L. Stephens, K. Chan, C. Hahn, J. K. Nørskov, T. F. Jaramillo and I. Chorkendorff, *Chem. Rev.*, 2019, **119**, 7610–7672.
2. S. Garg, M. Li, A. Z. Weber, L. Ge, L. Li, V. Rudolph, G. Wang, and T. E. Rufford, *J. Mater. Chem. A.,* 2020, **8**, 1511–1544.
3. R. G. Mariano, K. Mckelvey, H. S. White and M. W. Kanan, *Science,* 2017, **358,** 1187–1192.
4. J. J. Lv, M. Jouny, W. Luc, W. Zhu, J. J. Zhu, and F. Jiao, *Adv. Mater.*, 2018, **30**, 1803111.
5. W. Choi, Y. Choi, E. Choi, H. Yun, W. Jung, W. H. Lee, H. S. Oh, D. H. Won, J. Na, and Y. J. Hwang, *J. Mater. Chem. A,* 2022, **10** 10363–10372.
6. K. P. Kuhl, T. Hatsukade, E. R. Cave, D. N. Abram, J. Kibsgaard and T. F. Jaramillo, *J. Am. Chem. Soc.,* 2014, **136**, 14107–14113.
7. D. N. Celada, and A. S. Varela, *J. Mater. Chem. A,* 2022, **10,** 5899–5917.
8. D. Gao, I. Zegkinoglou, N. J. Divins, f. Scholten, I. Sinew, P. Grosse, and B. R. Cuenya, *ACS Nano*, 2017, **11**, 4825–4831.
9. C. Chen, X. Yan, S. Wu, S. Liu, X. Sun, Q. Zhu, R. Feng, T. Wu, Q. Qian, H. Liu, L. Zheng, J. Zhang, and B. Han*, Chem. Sci.,* 2021, **12**, 5938–5943. A
10. D. Ren, Y. Deng, A. D. Handoko, C. S. Chen, S. Malkhandi, and B. S. Yeo, *ACS Catal.*, 2015, **5**, 2814–2821.
11. J. Li, A. Ozden, M. Wan, Y. Hu, F. Li, Y. Wang, R. R. Zamani, D. Ren, Z. Wang, Y. Xu, D. H. Nam, J. Wicks, B. Chen, X. Wang, M. Luo, M. Graetzel, F. Che, E. H. Sargent, and D. Sinton*, Nat. Commun.*, 2021, **12**, 1–10.
12. H. Yun, W. Choi, D. Shin, H. S. Oh, and Y. J. Hwang, *ACS Catal.*, 2023, **13**, 9302–9312.
13. C. P. O'Brien, R. K. Miao, S. Liu, Y. Xu, G. Lee, A. Robb, J. E. Huang, K. Xie, K. Bertens, C. M. Gabardo, J. P. Edwards, C. T. Dinh, E. H. Sargent, and D. Sinton, *ACS Energy Lett*., 2021, **6**, 2952–2959.
14. C. W. Lee, S. J. Shin, H. Jung, D. L. T. Nguyen, S. Y. Lee, W. H. Lee, D. H. Won, M. G. Kim, H. S. Oh, T. Jang, H. Kim, B. K. Min, and Y. J. Hwang, *ACS Energy Lett.,* 2019, **4**, 2241–2248.
15. A. Xu, S. F. Hung, A. Cao, Z. Wang, N. Karmodak, J. E. Huang, Y. Yan, A. S. Rasouli, A. Ozden, F. Y. Wu, H. J. Tsai, T. J. Lee, F. Li, M. Luo, Y. Wang, X. Wang, J. Abed, Z. Wang, D. H. Nam, Y. C. Li, A. H. lp, D. Sinton, C. Dong, and E. H. Sargent, *Nat. Catal.*, 2022, **5**, 1081–1088.
16. X. Li, Q. Lium, J. Wang, D. Meng, Y. Shu, X. Lv, B. Zhao, H. Yang, T. Cheng, Q. Gao, L. Li, and H. B. Wu, *Chem*, 2022, **8**, 2148–2162.
17. Y. Kamimura and A. Endo, *Phys. Chem. Chem. Phys.*, 2016, **8**, 2699–2709.
18. T. Joutsuka and S. Tada, *J. Phys. Chem. C*, 2013, **127** 6998–7008.
19. N. Scotti, F. Bossola, F. Zaccheria, and N. Ravasio, *Catalysts,* 2020, **10**, 168.
20. N. S. Mclntyre, and M. G. Cook, *Anal. Chem.,* 1975, **47**, 2208–2212.
21. M. C. Biesinger, L. W. M. Lau, A. R. Gerson, and R. St. C. Smart, *Appl. Surf. Sci.,* 2010, **257**, 887–898.
22. M. Shaw, D. Samanta, S. Bera, M. K. Mahto, M. A. S. Shaik, S. Konar, I. Mondal, D. Dhara, and A. Pathak, *Inorg. Chem.,* 2022, **61**, 14568–14581.
23. J. L. Colón, D. S. Thakur, C. Y. Yang. A. Clearfield, and C. R. Martini, *J. Catal.*, 1990, **124**, 148–159.
24. A. Gaur, and B. D. Shrivastava, *Acta Phys. Pol., A,* 2012, **121**, 647–652.
25. W. Sun, Y. Song, X. Gong, L. Cao, and J. Yang, *Chem. Sci.*, 2015, **6**, 4993–4999.
26. H. Funke, M. Chukalina, and A. Rossberg, *Phys. Scr.*, 2005, **115**, 232–234.
27. J. Timoshenko, and A. Kuzmin, *Comput. Phys. Commun.*, 2009, **180**, 920–925.
28. Y. W. Han, L. Ye, T. J. Gong, X. B. Lu, and Y. Fu, *Adv. Funct. Mater.*, 2024, **34**, 2315044.
29. Z. Li, Z. Liu, S. Li, Y. Pei, D. Li, J. Mao, R. Zhou, C. Qiu, Y. Lu, and B. Zhang, *J. Mater. Chem. A,* 2024, **12**, 15082–15089.
30. V. Sudha, G. Murugadoss, and R. Thangamuthu, *Sci. Rep.,* 2021, **11**, 3413.
31. O. Seiferth, K. Wolter, B. Dillmann, G. Klivenyi, H. J. Freund, D. Scarano, and A. Zecchina, *Surf. Sci.,* 1999, **421**, 176–190.
32. C. Zhu, A. Osherov, and M. J. Panzer*., Electrochim. Acta*, 2013, **111**, 771–778.
33. W. N. R. W. Isahak, Z. A. C. Ramli, M. W. Ismail, K. Ismail, R. M. Yusop, M. W. M. Hisham, and M. A. Yarmo, *J. CO2 Util.,* 2013, **2**, 8–15.
34. X. Wang, Q. Chen, Y. Zhu, K. Wang, Y. Chang, X. Wu, W. Bao, T. Cao, H. Chen, Y. Zhang, and H. Qin, *Signal Transduction Targeted Ther.*, 2023, **8**, 277.
35. M. Burachevskaya, T. Minkina, S. Mandzhieva, T. Bauer, D. Nevidomskaya, V. Shuvaeva, S. Suchkova, R. Kizilkaya, C. Gülser, and V. Rajput, *Environ. Geochem. Health*, 2021, **43**, 1655–1672.